High Contrast Impedance Tomography

Liliana Borcea*, James G. Berryman† and George C. Papanicolaou‡

May 9, 1996

Abstract

We introduce an output least-squares method for impedance tomography problems that have regions of high conductivity surrounded by regions of lower conductivity. The high conductivity is modeled on network approximation results from an asymptotic analysis and its recovery is based on this model. The smoothly varying part of the conductivity is recovered by a linearization process as is usual. We present the results of several numerical experiments that illustrate the performance of the method.

Contents

1 Introduction **1**

2 The High Contrast Model **2**
2.1 Description of the Model 2
2.2 Review of the Asymptotic Theory 2

3 Inversion Algorithm **4**
3.1 Identification of the Asymptotic Resistor Network 4
3.2 Identification of Features of the Conductivity that are Neglected by the Asymptotic Theory 6

4 Numerical Results **7**
4.1 The PLTMG Solver 7
4.2 One Channel Model 7
4.3 Nonuniform Background 11
4.4 Multiple Channels 13

5 Physical Interpretation of Single Channel Inversion **15**

6 Summary **18**

*Scientific Computing and Computational Mathematics, Stanford University, Stanford, CA 94305, email: borcea@sccm.stanford.edu

†Lawrence Livermore National Laboratories, Earth Sciences Division, P. O. Box 808 L-202, Livermore, CA 94551-9900, email: berryman@s123.es.llnl.gov

‡Dept of Mathematics, Stanford University, Stanford, CA 94305, email: papanico@math.stanford.edu

1 Introduction

Let Ω be a bounded two-dimensional region with conductivity $\sigma(x,y)$ and resistance (or impedance) $\rho(x,y) = \frac{1}{\sigma(x,y)}$. The recovery of σ from measurements of the potential ϕ at the boundary $\partial\Omega$ is the impedance tomography problem. The potential ϕ is the solution of the boundary value problem

$$\begin{aligned} \nabla \cdot (\sigma \nabla \phi) &= 0 \quad \text{in} \quad \Omega \\ \sigma \frac{\partial \phi}{\partial n} &= I \quad \text{on} \quad \partial\Omega, \end{aligned} \tag{1.1}$$

where the imposed surface current density I satisfies $\int_{\partial\Omega} I dS = 0$ and the potential ϕ is unique up to a constant. When the conductivity σ is sufficiently smooth and the full Neumann to Dirichlet map is known, that is, measurements of ϕ are given on $\partial\Omega$ for all possible current source distributions I, then it is known that the conductivity can be recovered in principle [29, 43, 44]. An extensive review of the uniqueness and stability of the impedance tomography problem is given in [24]. There is also an extensive literature on recovery algorithms, based mostly on linear output least-squares methods, that work well for low contrast or linearized conductivity problems [1, 7, 17, 25, 37, 40, 42, 46]. Electromagnetic impedance tomography, in which σ in (1.1) is complex valued, is also of interest in geophysical applications [3, 4] but there is relatively little theoretical development for it at present. In this paper we consider the impedance tomography problem with static (d.c.) boundary excitation and real valued conductivity. A possible configuration of current sources and points where the potential is measured, on part of the boundary of a square region, is shown in Fig. 1.1.

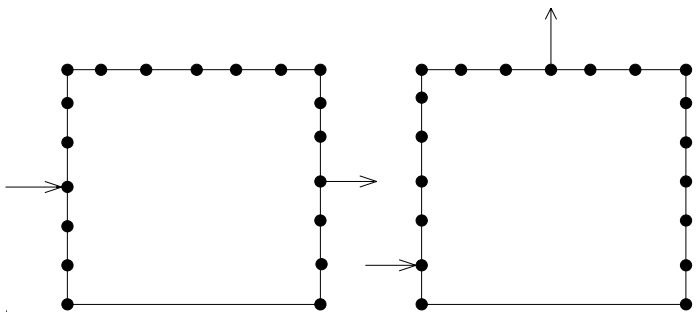

Figure 1.1: An impedance tomography problem for a square region Ω. Showing two current injection patterns, where the arrows represent current sources and the dots represent points where the potential is measured.

We consider the recovery of the conductivity from boundary measurements when there are regions of high contrast so that linearization methods (the Born approximation) do not work. The analysis of current flow in regions with high conductivity, the direct problem, has been carried out in [30, 13]. This analysis motivates our approach to the high contrast inverse problem: we model the unknown conductivity in a special way, suggested by the analysis of the direct problem, and then estimate the parameters of the model conductivity by an output least-squares process.

In the next section we give a brief review of the analysis of high contrast conductivity problems. In section 3 we describe the inversion algorithm that we use for estimating high contrast conductivities and in section 4 we present results from numerical computations based on this algorithm. In section 5 we explain briefly why the approach we follow works. In section 6 we provide a short summary and conclusions.

2 The High Contrast Model

2.1 Description of the Model

There are many ways in which high contrast conductivity may arise in practice. We can have, for example, a uniform background conductivity with highly conducting or insulating inclusions. Since in most potential applications we do not know the shape of the inclusions, it is convenient to assume that the high contrast of the conductivity (σ) arises in a general way from a continuum model of the form

$$\sigma(\mathbf{x}) = \sigma_0 e^{-S(\mathbf{x})/\epsilon}. \tag{2.1}$$

Here σ_0 is a constant reference conductivity, $S(\mathbf{x})$ is a smooth function and ϵ is a small parameter. Variations of the function $S(\mathbf{x})$, the scaled logarithm of the conductivity, are amplified by the parameter ϵ, producing the high contrast of the conductivity. Media with discontinuous conductivities, like ones with inclusions of finite size, can then be viewed as particular cases of the generic model (2.1).

2.2 Review of the Asymptotic Theory

In this section we review some of the results obtained in [30, 13] for transport in media with high contrast conductivity given by (2.1). Even though the analysis is done in the context of homogenization [8, 26] the conclusions are equally valid for more general circumstances.

We consider the flow problem

$$\nabla \cdot (\sigma \nabla \phi) = 0 \tag{2.2}$$

in a periodic unit cell Ω, where ϕ is the electric potential and $\sigma(\mathbf{x})$ is the conductivity. The flow is driven by the condition

$$< \nabla \phi >= \mathbf{e}, \tag{2.3}$$

where $< \cdot >$ stands for the normalized average over Ω and $\mathbf{e}$ is a unit vector. The mean potential gradient can be specified, for example, by prescribing two different constant potentials at opposite sides of the domain.

By using Ohm's law $\mathbf{j} = \sigma \nabla \phi$, where $\mathbf{j}$ is the electric current, we can also consider the dual problem

$$\begin{aligned} \nabla \times (\rho \mathbf{j}) &= 0 \\ \nabla \cdot \mathbf{j} &= 0 \\ < \mathbf{j} > &= \mathbf{e}, \end{aligned} \tag{2.4}$$

where $\rho(\mathbf{x}) = \sigma(\mathbf{x})^{-1}$ is the resistance.

It is shown in [30, 13] that when the conductivity has logarithmic high contrast in the form (2.1) there is strong channeling of the flow at the saddle points of σ. Moreover, by using the variational formulation of the effective conductivity and resistance [13]

$$\begin{aligned} \overline{\sigma} &= \min_{<\nabla\phi>=\mathbf{e}} < \sigma \nabla \phi \cdot \nabla \phi > \\ \overline{\rho} = \frac{1}{\overline{\sigma}} &= \min_{<\mathbf{j}>=\mathbf{e},\ \nabla\cdot\mathbf{j}=0} < \rho \mathbf{j} \cdot \mathbf{j} >, \end{aligned} \tag{2.5}$$

it is shown that, in the asymptotic limit of high contrast, the leading order term in the effective parameters $\overline{\sigma}$ and $\overline{\rho}$ is obtained by considering the flow only in the neighborhoods of the saddle points of σ.

To explain this flow behavior in the vicinity of the saddles, let us assume that the conductivity has a single saddle point $\mathbf{x}_S \in \Omega$, which is oriented in the driving direction, say $\mathbf{e} = \mathbf{e}_1 = (1,0)$. In a small neighborhood of $\mathbf{x}_S$, the conductivity has the form

$$\sigma(\mathbf{x}) \approx \sigma(\mathbf{x}_S) exp[\frac{k(x-x_S)^2}{2\epsilon} - \frac{p(y-y_S)^2}{2\epsilon}], \tag{2.6}$$

where k and p are the curvatures of $S(\cdot)$ at the saddle point. In general, the saddle point can be oriented in any direction but equation (2.6) still holds if, at $\mathbf{x}_S$, we introduce a local system of coordinates (x,y) such that the x direction coincides with the direction of the saddle. We take as the small region around $\mathbf{x}_S$ the square $\mid x - x_S \mid \leq \delta, \mid y - y_S \mid \leq \delta$ where the parameter $\delta \to 0$ in such a way that $\frac{\delta}{\epsilon} \to \infty$ as $\epsilon \to 0$.

From (2.2), the local problem near the saddle point is

$$\begin{aligned} \nabla \cdot \{\sigma(\mathbf{x}_S) exp[\frac{k(x-x_S)^2}{2\epsilon} - \frac{p(y-y_S)^2}{2\epsilon}] \nabla\phi\} = 0 \\ < \nabla\phi >= \mathbf{e}_1, \end{aligned} \tag{2.7}$$

which we solve by separation of variables. The potential $\phi(\mathbf{x})$ is

$$\phi(x,y) \approx \frac{1}{2} erf(\sqrt{\frac{k}{2\epsilon}}(x - x_S)), \tag{2.8}$$

correct up to an additive constant which is set to zero here. The analytical basis for (2.8) is matched asymptotic expansions. The local analysis gives the leading term (2.8) of the inner expansion valid near the saddle point. The outer expansion deals with the diffuse flow in the rest of the domain. The potential $\phi(\mathbf{x})$ therefore has the character of an inner layer in the direction of the saddle, the x direction in this case.

From (2.8) we compute the potential gradient

$$\nabla\phi(x,y) \approx \frac{1}{\sqrt{\frac{2\pi\epsilon}{k}}} e^{-\frac{k(x-x_S)^2}{2\epsilon}} \mathbf{e}_1 \tag{2.9}$$

and the current

$$\mathbf{j} = -\sigma\nabla\phi \approx -\frac{\sigma(\mathbf{x}_S)}{\sqrt{\frac{2\pi\epsilon}{k}}} e^{-\frac{p(y-y_S)^2}{2\epsilon}} \mathbf{e}_1. \tag{2.10}$$

We see from these expressions that when the contrast of σ is high (ϵ is small) both the current and the potential gradient are narrow Gaussians centered at $\mathbf{x}_S$, which means that there is strong flow channeling around the saddle point of the conductivity. The results (2.9) and (2.10) imply that the overall, or effective, conductivity and resistance (2.5) are (see [30, 13])

$$\overline{\sigma} \approx \sigma(\mathbf{x}_S)\sqrt{\frac{k}{p}} \quad \text{and} \quad \overline{\rho} \approx \frac{1}{\sigma(\mathbf{x}_S)}\sqrt{\frac{p}{k}}. \tag{2.11}$$

Thus, the flow through a medium with high contrast conductivity can be approximated by the flow through a resistor having resistance $\overline{\rho}$, given by (2.11).

In more general situations, where there are more saddle points of σ in the region that are oriented in different directions, the flow still concentrates at the saddles but it follows a more complicated

pattern, which is a network of channels. Locally, around each saddle point of the conductivity, the flow is approximated by the current through resistors given by (2.11). These resistors are connected in a network that is identified as follows: the nodes of the network are the maxima of $\sigma(\mathbf{x})$ and the branches are paths connecting two adjacent maxima over a saddle point. A detailed analysis is given in [13].

3 Inversion Algorithm

The asymptotic network theory described in §2 suggests that if we have flow channeling in the medium that we are trying to image, there is significant information in the data about the resistor network that describes the flow in the high contrast regions of the conductivity. Thus, in the first step of the inversion algorithm, we should attempt to identify the resistor network (channels of flow). The flow through this network is also the leading order term of the flow in the high contrast regions of σ. We can then use the conductivity estimate from the first stage of the inversion algorithm as a starting point for the second stage, in which we try to recover other features that were not captured by the network. In this step of the inversion we can linearize about the conductivity of the resistor network. Linearization works well at this stage because the main part of the flow through the high contrast regions of σ is already estimated, and small changes of the conductivity about it produce only small changes in the potential gradients.

3.1 Identification of the Asymptotic Resistor Network

In order to identify the resistor network that describes the flow through the high contrast regions, we *model* the unknown conductivity σ by

$$\sigma(\mathbf{x}) \longrightarrow \sigma_b + \sum_{j=1}^{m} \chi_j(\mathbf{x}, \mathbf{s}_j) f_j(\mathbf{x}, \mathbf{s}_j). \tag{3.1}$$

Here σ_b is a uniform background in which we imbed the high contrast modules $f_j(\cdot)$. Each high contrast module is of the form $f_j(\cdot) \sim e^{\frac{S_j(\mathbf{x})}{\epsilon}}$, with support in the interior of Ω, and consists of a saddle point surrounded by two maxima and two minima. The vectors of parameters $\mathbf{s}_j$ describe the structure of the modules $f_j(\cdot)$ by specifying the position of the saddle points, their orientation, the curvatures at the saddle, the contrast, etc. The modules $f_j(\cdot)$ are localized with the smooth cutoff functions $\chi_j(\cdot)$. Detailed descriptions are given in section 4.2.

Since conductivities defined by (3.1) are completely determined by the parameters $\mathbf{s}_j$, $j = 1, \ldots m$, we estimate them by minimizing the error between the solution with these parameters and the observed data. Thus, we estimate the $\mathbf{s}_j$, $j = 1, \ldots m$ by minimizing the mean-square error

$$E(\mathbf{s}_1, \ldots \mathbf{s}_m) = \sum_{i=1}^{M} \sum_{k=1}^{N} [\psi_k^{(i)} - \phi_k^{(i)}(\mathbf{s}_1, \ldots \mathbf{s}_m)]^2, \tag{3.2}$$

where the index of summation k runs through the data points on the boundary and i labels the pair of electrodes at which the current is injected into the domain. The potential measured on the boundary is $\psi_k^{(i)}$, while $\phi_k^{(i)}(\cdot)$ is the potential on the boundary calculated by solving the partial differential equation (1.1) with the current best estimate of a conductivity of the form (3.1). This is an output least-squares estimation method, parametrized with high contrast conductivities of the form (3.1).

Introducing a model of the form (3.1) for the conductivity is a form of *regularization* [45, 34, 35, 32] for the output least squares problem (3.2). It is particularly well suited to high contrast problems, as we know from the analysis of the direct problem summarized in section 2.2.

To describe the minimization algorithm that we use, we assume for simplicity that we have only one high contrast module ($m = 1$) in (3.1). When the vector of parameters $\mathbf{s} \in \mathbb{R}^p$ changes by $\Delta\mathbf{s}$, the mean-square error (3.2) changes by

$$E(\mathbf{s}) + \Delta E \approx \sum_{i=1}^{M}\sum_{k=1}^{N}[\psi_k^{(i)} - \phi_k^{(i)}(\mathbf{s}) - \sum_{j=1}^{p}\frac{\partial\phi_k^{(i)}}{\partial s_j}\Delta s_j]^2, \tag{3.3}$$

where we use the fact that, when the change in $\mathbf{s}$ is small, we have

$$\phi_k^{(i)}(\mathbf{s} + \Delta\mathbf{s}) \approx \phi_k^{(i)}(\mathbf{s}) + \sum_{j=1}^{p}\frac{\partial\phi_k^{(i)}}{\partial s_j}\Delta s_j. \tag{3.4}$$

From (3.3) the change in the error is

$$\Delta E \approx \sum_{j=1}^{p}\sum_{l=1}^{p}A_{jl}\Delta s_j\Delta s_l - 2\sum_{j=1}^{p}b_j\Delta s_j. \tag{3.5}$$

Here we introduced the symmetric positive definite sensitivity matrix

$$A_{jl} = \sum_{i=1}^{M}\sum_{k=1}^{N}\frac{\partial\phi_k^{(i)}}{\partial s_j}\frac{\partial\phi_k^{(i)}}{\partial s_l} \tag{3.6}$$

and the vector

$$b_j = \sum_{i=1}^{M}\sum_{k=1}^{N}[\psi_k^{(i)} - \phi_k^{(i)}(\mathbf{s})]\frac{\partial\phi_k^{(i)}}{\partial s_j}, \tag{3.7}$$

whose components measure the current data misfit weighted by the sensitivity of the potential to changes in s_j. The decrease in the error ΔE is maximized when the parameters $\Delta\mathbf{s}$ satisfy the linear equations

$$A\Delta\mathbf{s} = \mathbf{b} \tag{3.8}$$

and then the change in the mean-square error is

$$\Delta E \approx -\Delta\mathbf{s}^T A\Delta\mathbf{s} \leq 0. \tag{3.9}$$

This Gauss-Newton algorithm [21, 18, 20], given by (3.6) - (3.8), does not work well here because the matrix A, defined by (3.6), is ill-conditioned. Some of the components of the parameter vector $\mathbf{s}$ change faster than others. For example, when the contrast is high and the flow concentration at the saddle point is strong, the position of the saddle point is recovered after a few iterations while the contrast converges slowly. We avoid this difficulty by updating the vector of parameters $\mathbf{s}$ one component at a time, instead of all at once. This approach has, in addition, the advantage of allowing us to terminate the updating of parameters that have converged before the end of the overall iteration process. The change in the j^{th} component of $\mathbf{s}$ that maximizes the decrease in the error is easily found to be

$$\Delta s_j = \frac{\sum_{i=1}^{M}\sum_{k=1}^{N}[\psi_k^{(i)} - \phi_k^{(i)}(\mathbf{s})]\frac{\partial\phi_k^{(i)}}{\partial s_j}}{\sum_{i=1}^{M}\sum_{k=1}^{N}(\frac{\partial\phi_k^{(i)}}{\partial s_j})^2} = \frac{b_j}{A_{jj}} \tag{3.10}$$

and then

$$\Delta E \approx -(\Delta s_j)^2 \sum_{i=1}^{M} \sum_{k=1}^{N} (\frac{\partial \phi_k^{(i)}}{\partial s_j})^2 = -A_{jj}(\Delta s_j)^2 \leq 0. \tag{3.11}$$

The change in the parameters $\mathbf{s}$ depends both on the error at the boundary and on the sensitivity coefficients $\frac{\partial \phi_k^{(i)}}{\partial s_j}$. Thus, at each step of the iteration we must solve the elliptic problems

$$\begin{aligned} \nabla \cdot (\sigma \nabla \phi) &= 0 \\ \sigma \frac{\partial \phi}{\partial n} &= f \text{ on } \partial\Omega \\ \phi(\mathbf{0}, \mathbf{s}) &= 0 \end{aligned} \tag{3.12}$$

and

$$\begin{aligned} \nabla \cdot (\sigma \nabla \frac{\partial \phi}{\partial s_i}) &= -\nabla \cdot (\frac{\partial \sigma}{\partial s_i} \nabla \phi) \\ \sigma \frac{\partial}{\partial n} (\frac{\partial \phi}{\partial s_i}) &= 0 \text{ on } \partial\Omega \\ \frac{\partial \phi}{\partial s_i}(\mathbf{0}, \mathbf{s}) &= 0 \text{ for } i = 1, \ldots p. \end{aligned} \tag{3.13}$$

However, since small changes in the components of $\mathbf{s}$ lead to an updated potential of the form (3.4), we need not solve (3.12) for each iteration but only once every p iterations.

In the Gauss-Newton method used here we approximate the Hessian of the mean square error (3.1) by the first derivatives of the estimated potential (3.4). We omit the second derivatives which are difficult to calculate. The success of the method depends on the negligibility of second derivatives [18, 20, 21] and to insure that they are negligible, we scale the update in the parameters (3.10) by a factor $\lambda_c > 0$. The algorithm then called damped Gauss-Newton methods [18, 21] is globally convergent for many nonlinear least-squares problems, including large residual problems [18, 21]. In our computations we choose the scaling parameter λ_c so that the change in s_j is smaller than 15%.

3.2 Identification of Features of the Conductivity that are Neglected by the Asymptotic Theory

The resistor network identified by the algorithm described in §3.1 is in general only a rough estimate of the conductivity $\sigma(\mathbf{x})$. In order to improve its resolution we must also identify low contrast features of $\sigma(\mathbf{x})$ that are not captured by the asymptotic resistor network theory. This is done by linearizing about the network conductivity estimated by the algorithm described in the previous section. In this section we define the linearized problem and explain why it works at this stage of the inversion algorithm.

For a reference medium with conductivity $\sigma_r(\mathbf{x})$ of form (3.1), we have

$$\begin{aligned} \nabla \cdot [\sigma_r(\mathbf{x}) \nabla \phi_r(\mathbf{x})] = 0 \quad \text{in} \quad \Omega \\ \sigma_r \frac{\partial \phi_r}{\partial n} = I \quad \text{on} \quad \partial\Omega, \end{aligned} \tag{3.14}$$

where $\phi_r(\mathbf{x})$ is the reference potential. Suppose that

$$\sigma(\mathbf{x}) = \sigma_r(\mathbf{x}) + \delta\sigma(\mathbf{x}), \quad \text{where} \quad |\, \delta\sigma(\mathbf{x}) \,| \ll |\, \sigma_r(\mathbf{x}) \,| \,. \tag{3.15}$$

Then problem (1.1) can then be written as

$$\begin{aligned} \nabla \cdot [\sigma_r(\mathbf{x}) \nabla \psi(\mathbf{x})] &= -\nabla \cdot [\delta\sigma(\mathbf{x}) \nabla \phi(\mathbf{x})] \quad \text{in } \Omega \\ (\sigma + \delta\sigma) \frac{\partial \phi}{\partial n} &= I \quad \text{on } \partial\Omega, \end{aligned} \tag{3.16}$$

where $\psi(\mathbf{x}) = \phi(\mathbf{x}) - \phi_r(\mathbf{x})$. The perturbed potential gradient $\nabla\psi(\mathbf{x})$ that is due to the change $\delta\sigma(\mathbf{x})$ of the reference conductivity is assumed to be much smaller than the reference potential gradient $\nabla\phi_r(\mathbf{x})$, so we linearize (3.16)

$$\nabla \cdot [\sigma_r(\mathbf{x}) \nabla \psi(\mathbf{x})] \approx -\nabla \cdot [\delta\sigma(\mathbf{x}) \nabla \phi_r(\mathbf{x})] \quad \text{in } \Omega. \tag{3.17}$$

Equation (3.17) is linear in $\delta\sigma(\mathbf{x})$. Linearization is justified in the second stage of our inversion algorithm because, as we explained in §2.2, the resistor network given by $\sigma_r(\mathbf{x})$ determines the main part of the flow in the high contrast regions of the medium. Small changes of the reference conductivity can only produce small changes in the potential gradient, so linearization (3.17) can be used.

Inversion of the linearized problem (3.17), that is recovery of $\delta\sigma(\mathbf{x})$, has been the topic of numerous studies and an extensive literature on recovery algorithms is available [1, 7, 17, 25, 37, 40, 42, 46]. In our computations we used an adjoint representation [39] that requires less computation than the usual algorithms that are based on Green's functions.

4 Numerical Results

4.1 The PLTMG Solver

We review a few facts about the software package PLTMG [5] that we use for solving the elliptic problems (3.12) and (3.13) during the iterative process described in §3. PLTMG is an elliptic partial differential equation solver in two dimensions. It uses an adaptive multigrid approach and a finite element discretization based on continuous piecewise linear triangular elements.

We extensively tested the performance of PLTMG for problems of form (3.12) with high contrast conductivity in [14]. We found that for contrasts no higher than $O(10^2)$, the numerical solution given by PLTMG is accurate, within a few percent. When the contrast is higher, the solution produced by PLTMG can be quite inaccurate in the vicinity of the saddle points of σ where strong flow channeling occurs, but overall remains satisfactory away from the channels. Since in our computations we use only the boundary values of the potential and we assume that all the channels are in the interior of Ω, we may use PLTMG for computing the potential $\phi(\mathbf{x}, \mathbf{s})$ and the sensitivity coefficients $\frac{\partial \phi}{\partial s_i}(\mathbf{x}, \mathbf{s})$, $i = 1, \ldots p$, on the boundary.

4.2 One Channel Model

In this section we present numerical results obtained with the inversion algorithm described in §3 for conductivities that have only one saddle point in the domain. An example of such a conductivity is

$$\sigma(\mathbf{x}) = \sigma_b + \chi(\mathbf{x}, \mathbf{s}) f(\mathbf{x}, \mathbf{s}), \tag{4.1}$$

where σ_b is a uniform background $f(\cdot)$ is a high contrast module that has a saddle point surrounded by two maxima and two minima and $\chi(\cdot)$ is a cutoff function that localizes $f(\cdot)$. We model the

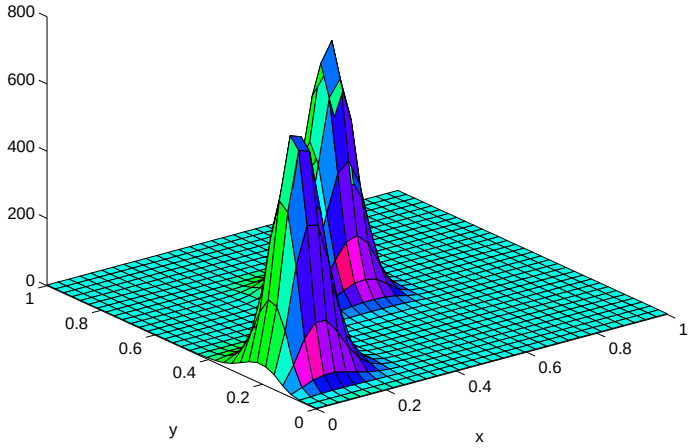

Figure 4.1: Model conductivity (Contrast = 369)

high contrast module by

$$f(\mathbf{x},\mathbf{s}) = \sigma_0 exp\{\frac{1}{\epsilon}\sin[\alpha((x-x_s)\cos\theta + (y-y_s)\sin\theta)]\sin[\beta((y-y_s)\cos\theta - (x-x_s)\sin\theta)]\}, \quad (4.2)$$

where (x_s, y_s) is the location of the saddle point of the conductivity, θ is the orientation of the saddle and ϵ determines the contrast. The function $f(\cdot)$ in (4.2) is periodic with periods determined by α and β, which also determine the curvatures at the saddle. The constant σ_0 controls the height of the saddle. Thus, the high contrast conductivity module is completely described by the eight-component vector

$$\mathbf{s} = (\sigma_b, \sigma_0, \alpha, \beta, x_s, y_s, \theta, \epsilon). \quad (4.3)$$

The high contrast module $f(\cdot)$ is tapered with the C^1 cutoff function

$$\chi(\mathbf{x},\mathbf{s}) = g((x-x_s)\cos\theta + (y-y_s), \alpha)g(-(x-x_s)\sin\theta + (y-y_s)\cos\theta), \beta), \quad (4.4)$$

where

$$g(\xi,\gamma) = \begin{cases} \sin^3[\frac{\pi}{2}(\xi + \frac{\pi}{\gamma})/d] & \text{for} \quad -\frac{\pi}{\gamma} \le \xi \le -\frac{\pi}{\gamma} + d \\ -\sin^3[\frac{\pi}{2}(\xi - \frac{\pi}{\gamma})/d] & \frac{\pi}{\gamma} - d \le \xi \le \frac{\pi}{\gamma} \\ 1 & -\frac{\pi}{\gamma} + d \le \frac{\pi}{\gamma} - d \\ 0 & \mid \xi \mid \ge \frac{\pi}{\gamma}. \end{cases} \quad (4.5)$$

The parameter d in (4.5) controls the sharpness of the cutoff and it is kept constant throughout the numerical experiments.

The data that we use in the numerical experiments are generated numerically with a synthetic model of the form (4.1) and PLTMG. An example of a conductivity used to generate data is shown in Fig. 4.1. In a uniform background, $\sigma_b = 2$, we have embedded a high contrast module ($\max(\sigma)/\min(\sigma) = 369$) that has a saddle at $(x_s, y_s) = (0.3, 0.4)$ which is oriented at an angle $\pi/4$ from the axes.

As a starting point in the iterative process of reconstructing the model σ shown in Fig. 4.1, we consider the conductivity shown in Fig. 4.2. Even though the initial guess is of the same form (4.1)

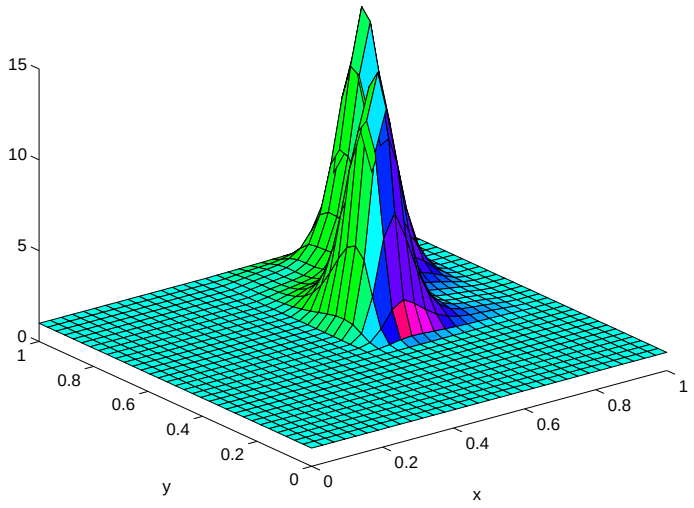

Figure 4.2: Initial conductivity guess (Contrast = 14.7)

as the model, the set of parameters $\{\mathbf{s}\}$ describing it is very different. The background conductivity is $\sigma_b^{init} = 1$; the saddle is situated at $(x_s, y_s)^{init} = (0.7, 0.7)$; and the contrast is 14.7. The initial relative error in the conductivity (see Fig. 4.3) is very high around the initial guess of the position of the saddle ($\sim 600\%$) and about 60% elsewhere in the domain.

In the reconstruction process, the data consists of the value of the potential at points placed a distance $h = 1/32$ apart along the sides ($x = 0$ and $x = 1$) and the surface boundary ($y = 1$). Current is injected with two different pairs of electrodes located at (0,0.5), (1,0.5) and (0,0.3), (0.5,1), respectively.

The evolution of the mean-square data error during the iteration process is shown in Fig. 4.4. The algorithm reduces this error monotonically. However, it does not guarantee reduction of the error in the conductivity and as shown in Fig. 4.5. At some stage of the iteration process the error in the model actually increases. This behavior is due to the strong nonlinearity of the problem and is more subdued in experiments with contrast of order ten. After 250 iterations, the relative error in the conductivity in the L_2 norm is reduced by two orders of magnitude. The final relative error in the model in the L_∞ norm (see Fig. 4.6) is only a few percent so the model conductivity is recovered quite well.

During the reconstruction process, some of the components of the vector of parameters $\mathbf{s}$ describing the model conductivity are recovered more quickly than others. For example, the position of the saddle point is expected to be easily recovered in experiments with high contrast. For low contrasts, flow channeling is weak so the position of the saddle is harder to recover. In Fig. 4.7 and 4.8, we show the evolution of the relative error in three parameters (ϵ, σ_b, and x_s) obtained from two numerical experiments that assume contrasts 10^4 and 14, respectively. As expected, when the contrast is high, the position of the saddle and the uniform background are recovered more quickly than the parameter ϵ that controls the contrast. However, when the contrast is lowered to 14 the position of the saddle is the last parameter to be recovered. The numerical experiment for reconstructing the model conductivity shown in Fig. 4.1 was repeated with data to which 5% noise has been added. The noise is simulated with independent, identically distributed Gaussian random variables. The starting point in the iteration is as before (see Fig. 4.2). From Fig. 4.9 we see

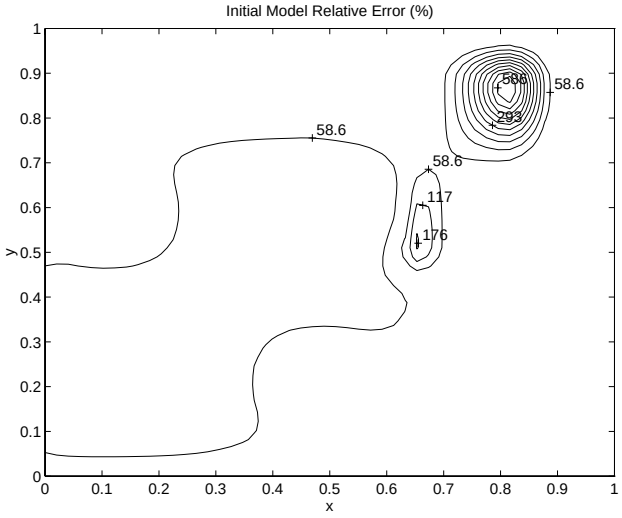

Figure 4.3: L_∞ initial relative error in the conductivity

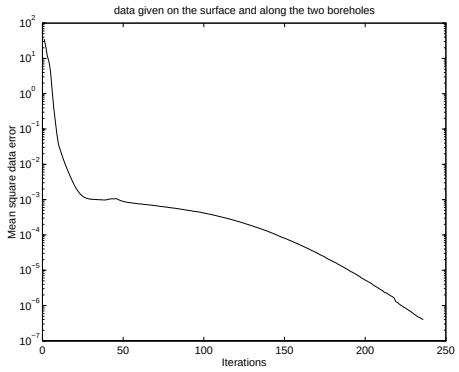

Figure 4.4: Evolution of the mean square data error

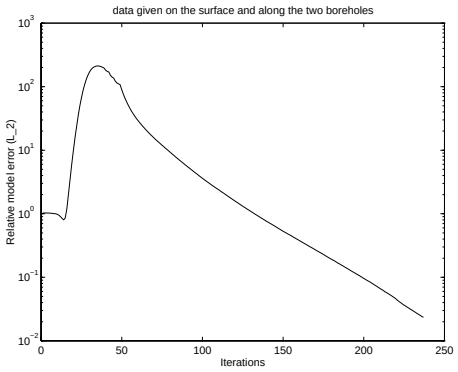

Figure 4.5: Evolution of the L_2 relative error in the conductivity

that the mean-square error decreases to about 10^{-2} in 50 iterations and remains unchanged after that. The relative error in the model in the L_∞ norm, shown in Fig. 4.10, tells us that, even with very noisy data, the algorithm recovers very well the background conductivity, the position and orientation of the channel and the support of the high contrast region. The error is high ($\sim 30\%$) only around the maxima of the conductivity where the potential gradient is nearly zero and so the inverse problem is ill-posed in this region. The quality of the results improves when the noise level is reduced. For example, with 1% noise the relative model error is smaller than 10%.

Since data are given only at a discrete number of points on the boundary, the resolution of the estimates is limited. To illustrate this point. we present the results of a numerical experiment with model conductivity in a tight, high contrast configuration. If the domain is discretized with a uniform mesh corresponding to the number of data points on the boundary, the distance between the two maxima of the high contrast conductivity is just six grid spacings. The contrast is 300 and the iteration starts, as before, with an initial guess that is far from the model parameters. The relative error in the conductivity at the end of the iteration process is shown in Fig. 4.11. Thus,

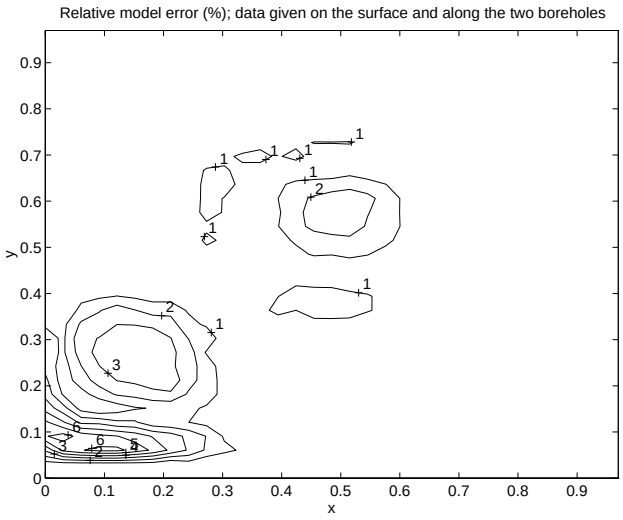

Figure 4.6: Relative model error (%)

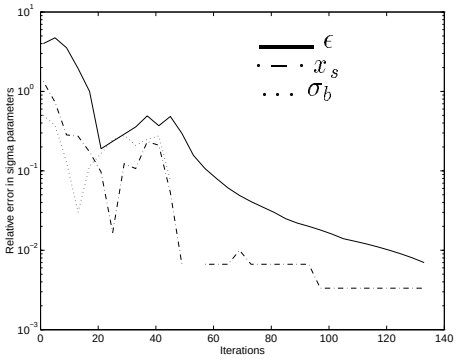

Figure 4.7: Convergence of high contrast module parameters. Contrast of $\sigma = 10^4$

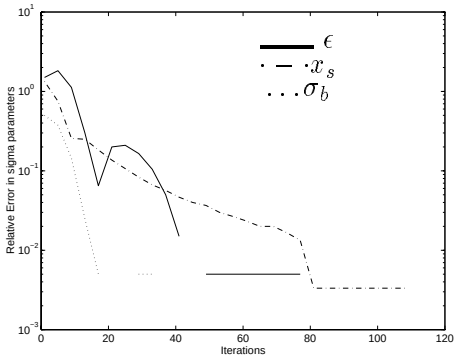

Figure 4.8: Convergence of high contrast module parameters. Contrast of $\sigma = 14$

the algorithm is successful in recovering the uniform background, the position and orientation of the channel, and the support of the high contrast region, but it does not give a very accurate conductivity around the position of the maxima.

4.3 Nonuniform Background

The numerical experiments presented so far show that the inversion algorithm described in §3.1 is successful in imaging the conductivity when the model σ belongs to the same class of functions (4.1) within which we are searching. We now consider a more realistic experiment in which we try to recover the model conductivity shown in Fig. 4.12, which consists of a high contrast module embedded in a variable background (see Fig. 4.13). The local variation in magnitude of the conductivity around the high contrast region is about 100, but only about 7 elsewhere in the domain. The data (ϕ at the boundary) are given at 32 uniformly distributed points along each side of the boundary and are generated numerically with the model conductivity shown in Fig. 4.12.

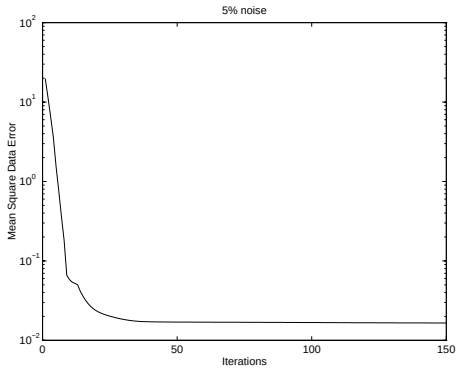

Figure 4.9: Evolution of mean square data error (5% noise)

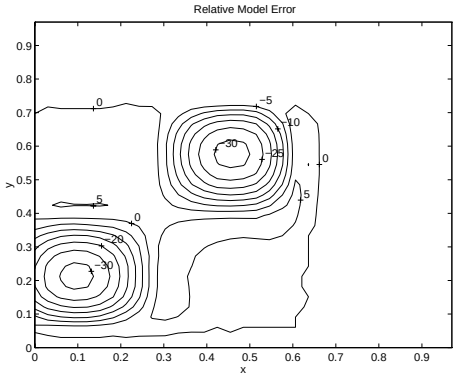

Figure 4.10: L_∞ conductivity error (5% noise)

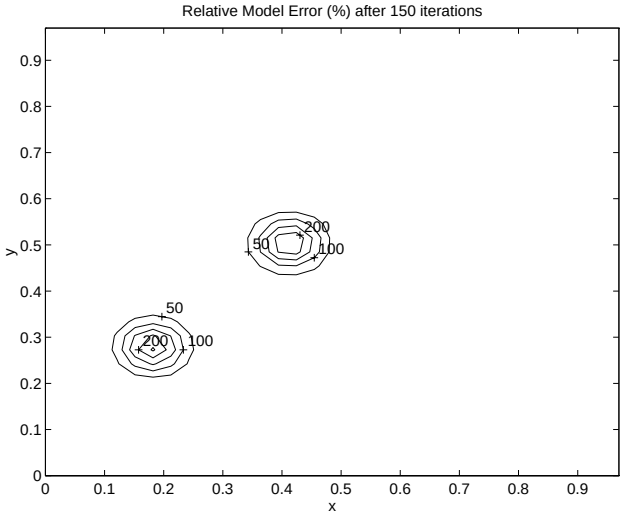

Figure 4.11: Tight high contrast configuration

In the first step of the inversion process, we looked for a conductivity of the form (4.1) that fits the data best. In the computations we consider data generated with only two pairs of electrodes at $(0., 0.5)$, $(1., 0.5)$ and $(0.5, 0.)$, $(0.5, 1.)$ respectively. The result is shown in Fig. 4.14 and the error in the conductivity is shown in Fig. 4.15 and 4.16. Thus, the inversion algorithm recovered the position and orientation of the channel as well as the support of the high contrast region. The error is large around the two peaks of the conductivity and for the background in which we embedded the high contrast module. We may view the results of this first step as a low resolution image of the conductivity, that gives only features that control the leading order term of the flow. Other details, like the variable background conductivity, are completely ignored.

In the second step of the inversion process, we improve the quality of the image by linearizing about the conductivity given in the first step. In the numerical computations, we use the same data points as before and many more pairs of electrodes for current injection. It is natural that in the first step of the inversion it is sufficient to consider data from only a few (two) current source-sink pairs while in the next step (the linearization process) we need data from many more current

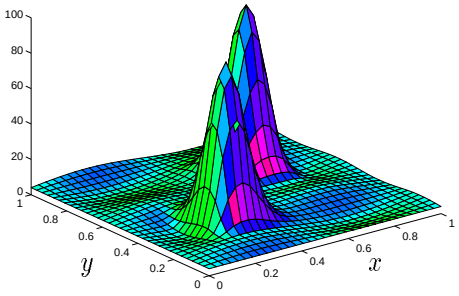

Figure 4.12: Model conductivity

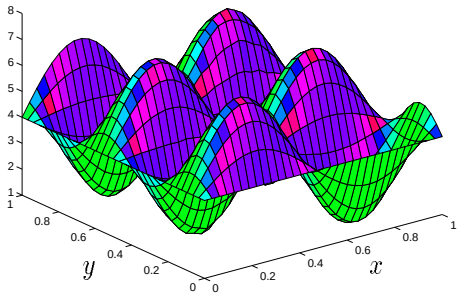

Figure 4.13: Background for the high contrast module

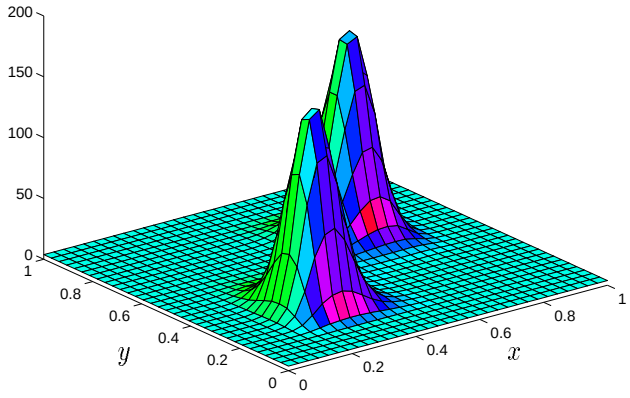

Figure 4.14: Conductivity after the first step of inversion

source-sink pairs. This simplification follows because the first inversion step looks only for the single channel of strong flow and, therefore, has only a few paramters to determine, while ignoring all other details of the conductivity. Thus, in order to get the single resistor in the asymptotic network, along with its position and orientation, we only need two current source-sink pairs into the domain, chosen so that flow will cross it.

The relative error of the final conductivity (Fig. 4.17) shows clearly that the quality of the image has improved in the background, by almost 150%. It remains constant around the peaks in the high contrast region of σ. The parameters identified in the first step of the inversion do not deteriorate during the linearization step.

4.4 Multiple Channels

All the numerical examples presented so far have a single channel of flow concentration in the medium. In general, there can be an arbitrary number of unknown channels. Identification of the resistor network in these cases can be done with the algorithm described in advance (§3.1), where the model conductivity will have many high contrast modules. Another approach is to identify a single channel at a time. We use this approach in imaging the conductivity of media with two and

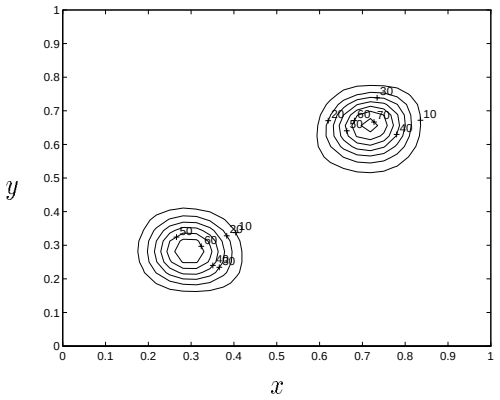

Figure 4.15: Absolute error in σ after the first step of the inversion

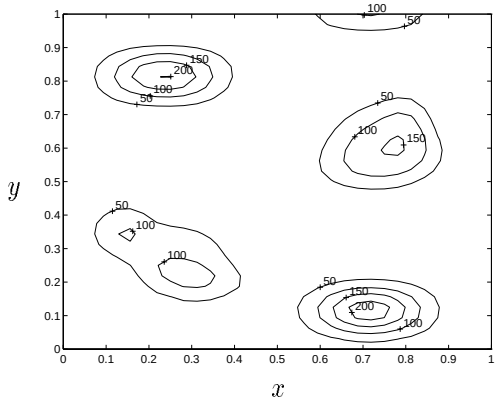

Figure 4.16: Relative error (%) in σ after the first step of the inversion

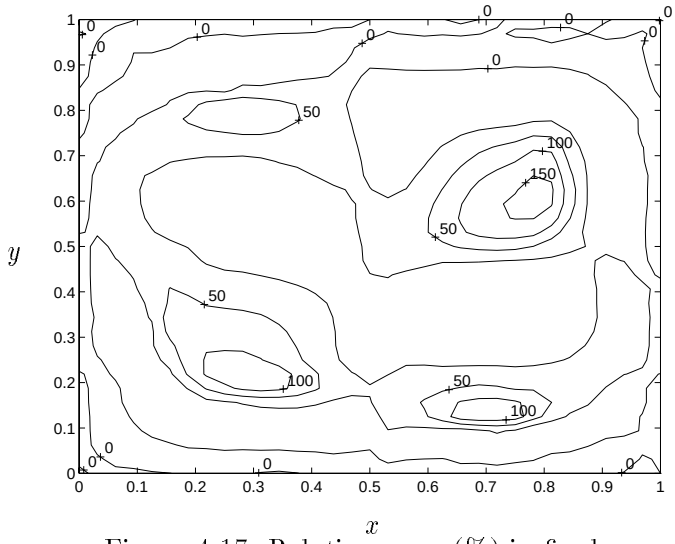

Figure 4.17: Relative error (%) in final σ

three channels of flow. If the channels are well separated, the algorithm works well. The channels are found sequentially, one by one, starting with the one closest to the boundary and ending with the ones in the interior of the flow domain.

The amount of data needed for inversion is larger than for media with a single channel of flow concentration, where data from two source-sink pairs are sufficient. For instance, in a numerical experiment with two channels we can recover the resistor network with six source-sink pairs. The error in the boundary data is shown with the dotted line in Fig. 4.18. The full line represents the error in an experiment with the same conductivity minus the interior channel and the same amount of data. We see that the error for the experiment with a single channel drops to 10^{-5}, while the error in the experiment with two channels has a more complex behavior. Initially, it decreases but then it stabilizes to a plateau at about 10^{-1}. This indicates that the algorithm has found the first channel and it cannot make any further reduction to the error unless a second high contrast module is introduced. The insertion of the second module is identified by the slight peak observed in the error around iteration 25. After this introduction, the error drops rapidly and then stabilizes at about 10^{-3}, which indicates that the second channel has been identified. The error is worse than

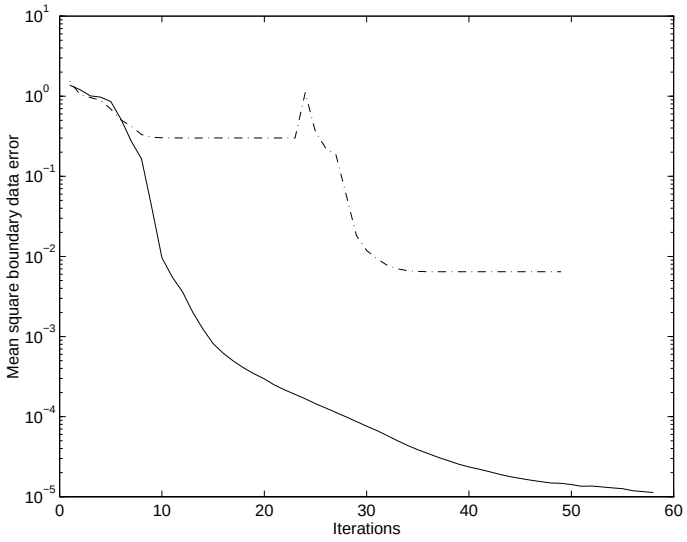

Figure 4.18: Output least-squares error as a function of the number of iterations. The solid lines is for conductivity function with one high contrast region. The dashed line is for a conductivity with two high contrast regions.

for the one channel experiment but it can be reduced by using more data.

The numerical experiments of this section show that when the medium consists of well separated channels of flow concentration, they can be identified one by one in a manner very similar to the method of matching pursuit [36]. However, when the channels are close together the algorithm breaks down because it tries to fit a high contrast module in between the channels. Such cases require special attention and will be considered in future research.

5 Physical Interpretation of Single Channel Inversion

In this section we explain why the inversion method of §3 is successful in finding the channels of flow inside the medium. We do this by identifying features in the boundary data that have channel information. We assume that the medium has a single channel and a conductivity that belongs to the class described by (4.1). The channel is oriented in the vertical direction and is located at $(0.7, 0.6)$ (see Fig. 5.1). The asymptotic theory (see §2.2) shows that the flow is concentrated around the channel and is diffuse elsewhere in the flow regime. Thus, when the boundary excitation is such that flow must pass through the channel, the potential gradient near it is a Gaussian centered at the saddle point and oriented in the vertical direction. The flow concentration in the interior of the medium is visible at those parts of the boundary that are relatively close to the channel.

For a current source located at $(0.5, 0.)$ and a sink at $(0.5, 1.)$, we plot in Fig. 5.2 the vertical potential gradient at the left and right boundaries of Ω. At the right boundary, which is closer to the saddle point, there is a maximum of the vertical potential gradient $(\nabla\phi \cdot \mathbf{e}_2)$ at $y = 0.6$. However, at the left boundary, which is farther away from the channel, flow concentration is not visible. When we drive the flow along the horizontal direction (source and sink are located at $(0., 0.5)$ and $(1., 0.5)$, respectively), the channel rejects the flow. Thus, the horizontal potential gradient has a minimum near the saddle point, which can be seen at the top boundary around $x = 0.7$ (see Fig

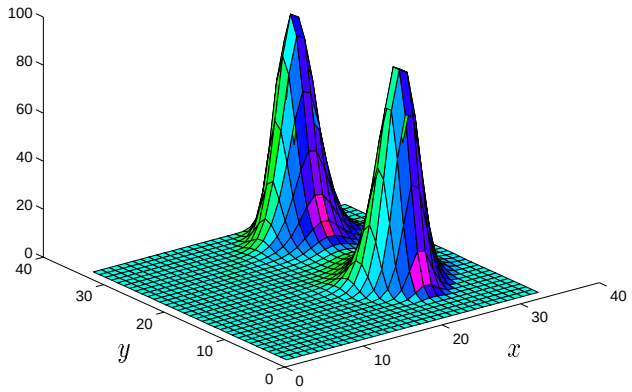

Figure 5.1: Conductivity with a vertical channel and uniform background

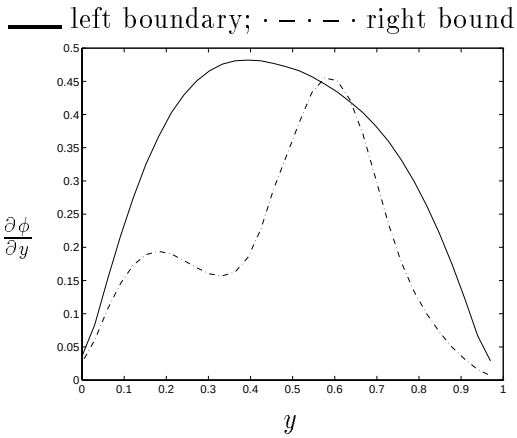

Figure 5.2: Vertical potential gradient at the left and right boundaries of Ω

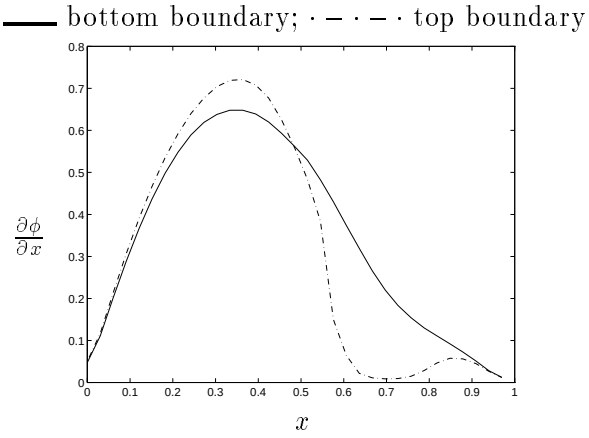

Figure 5.3: Horizontal potential gradient at the top and bottom boundaries of Ω

5.3). However, the minimum of $\nabla\phi \cdot \mathbf{e}_1$ cannot be observed at the bottom boundary, which is too far away from the channel. Thus, we can locate the vertical channel at $\mathbf{x}_S = (0.7, 0.6)$ very easily by just inspecting the boundary data.

The picture is more complicated when the high contrast module is embedded in a variable background because there are also regions of weak flow concentration in Ω that are felt at the boundary. For example, consider a medium with conductivity shown in Fig. 5.4. For a flow driven vertically with a current source and sink located at $(0.5, 0.)$ and $(0.5, 1.)$, respectively, the vertical potential gradient $(\nabla\phi \cdot \mathbf{e}_2)$ at the right and left boundaries is shown in Fig. 5.5. At the right boundary, we observe three maxima of the vertical potential gradient: one is centered at the saddle point $(y = 0.6)$ and the others (due to the minima of σ at $(0.75, 0.12)$ and $(0.83, 0.85)$) are centered at $y = 0.12$ and $y = 0.85$, respectively. At the left boundary, which is far from the saddle point, the channel is invisible but we observe two maxima of $\nabla\phi \cdot \mathbf{e}_2$. These maxima are due to the minima of the conductivity located at $(0.15, 0.31)$ and $(0.15, 0.75)$, respectively. When the sources are moved to $(0., 0.5)$ and $(1., 0.5)$, so that the flow has a horizontal direction, the channel at $\mathbf{x}_S = (0.7, 0.6)$ rejects the flow. In Fig. 5.6 we show the horizontal potential gradient $(\nabla\phi \cdot \mathbf{e}_1)$

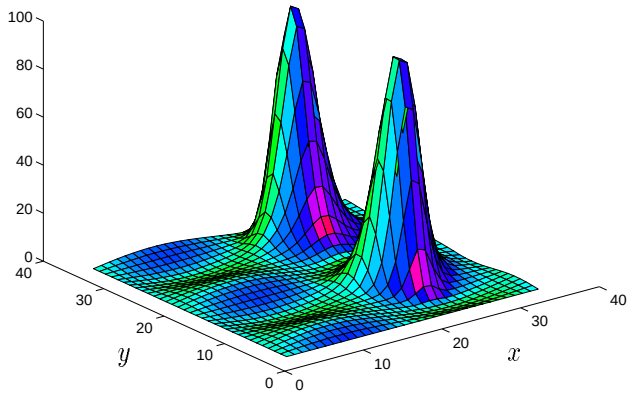

Figure 5.4: Conductivity with a vertical channel and variable background

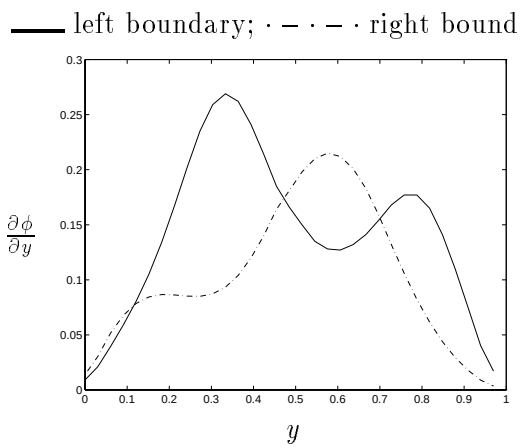

Figure 5.5: Vertical potential gradient at the left and right boundaries of Ω

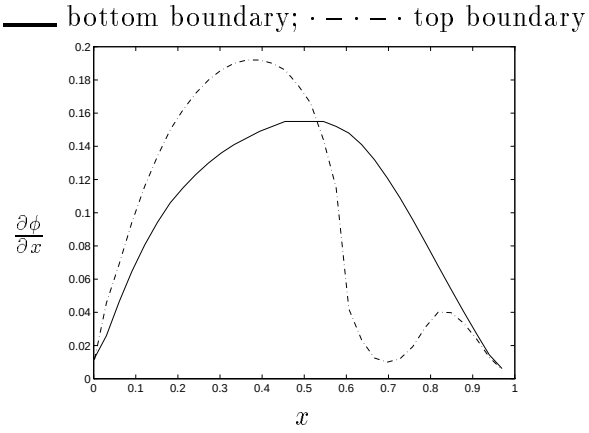

Figure 5.6: Horizontal potential gradient at the top and bottom boundaries of Ω

at the top and bottom boundaries. The top boundary is closer to the channel and the minimum of $\nabla\phi \cdot \mathbf{e}_1$ at $x = 0.7$ is evident. However, although the channel is not seen at the bottom boundary, we nevertheless observe the maxima of the horizontal potential gradient that are due to the minima of σ located at $(0.15, 0.31)$ and $(0.75, 0.15)$.

In general, the conductivity of the unknown medium has a complicated structure and finding its main features in the interior of Ω by inspection of the boundary data would be nearly impossible. Regions of weak flow concentration could give misleading information and channels can be hidden from the boundary. Consequently, the heuristic method for identifying channels in the medium described in this section is, in general, inefficient and inaccurate for complex situations. The simple examples presented here give, however, a physical explanation for the success of the inversion algorithm of §4 in localizing the channels in the medium.

6 Summary

We have introduced an inversion algorithm for tomographic imaging of media with large variations in the conductivity. The algorithm is based on the results of an asymptotic analysis of the forward problem in media with high contrast. This analysis shows that when the contrast of the conductivity is high, the flow can be roughly approximated by that of a resistor network. The network accounts for the main part of the flow and neglects the residual low contrast features of the conductivity. We introduce a new parametrization of the conductivity based on the resistor network theory and use an output least-squares approach for identifying the network. We have shown that this parametrization acts as a regularization for the inverse problem. The conductivity estimated in this first stage of the algorithm is used as a reference conductivity in a second stage, where we identify low contrast features that are not captured by the network.

We have assessed the performance of the algorithm with several numerical experiments and have shown that it is stable and successful in imaging high contrast conductivities in many situations. At present, the inversion algorithm uses high contrast modules that are somewhat rigid [see (4.1)-(4.5)], in the sense that they require the peaks of the conductivity surrounding the channel to have the same height. We are currently exploring less rigid models in order to eliminate this deficiency. Media with multiple channels of flow need to be explored further.

Acknowledgments

We thank F. Natterer for several useful discussions and for pointing out the use of adjoint representations for solving (3.13). The work of J. Berryman was performed under the auspices of the U. S. Department of Energy by the Lawrence Livermore National Laboratory under contract No. W-7405-ENG-48 and supported in part by the Geosciences Research Program of the DOE Office of Energy Research within the Office of Basic Energy Sciences, Division of Engineering and Geosciences. It was also supported in part by AFOSR grant F49620-94-1-0436. The work of L. Borcea and G. Papanicolaou was supported by NSF grant DMS96-22854 and AFOSR grant F49620-94-1-0436.

References

[1] Allen, A. and Santosa, F., 1991, *Stability and resolution analysis of a linearized problem in electrical impedance tomography*, Inverse Problems, **7**, pp. 515-533.

[2] Alessandrini, G., 1988,*Stable determination of conductivity by boundary measurements*, App. Anal., 27, pp. 153-172.

[3] Alumbaugh, D.L., Morrison, H. F., 1993,*Electromagnetic conductivity imaging with an iterative Born inversion*, IEEE Transactions on Geosciences and Remote Sensing, Vol. 31, No. 4, July, pp. 758-763.

[4] Alumbaugh, D.L. and Morrison, H.F., 1995, *Monitoring subsurface changes over time with cross-well electromagnetic tomography*, Geophysical Prospecting, **43**, pp. 873-902.

[5] Bank, E.R., 1990,*PLTMG: A Software Package for Solving Elliptic Partial Differential Equations*, SIAM.

[6] Banks, T.H. and Kunisch, K., 1989, *Estimation techniques for distributed parameter systems* (Boston Birkhaüser).

[7] Barber, D., Brown, B., 1986,*Recent developments in applied potential tomography-APT*, Information processing in medical imaging, Bacharach., S. ed., Nijhoff, Amsterdam, pp. 106-121.

[8] Bensoussan, A., Lions, J.L., Papanicolaou, G.C., 1978, *Asymptotic analysis for periodic structures*, North-Holland, Amsterdam.

[9] Berryman, J.G., 1990,*Stable iterative reconstruction algorithm for nonlinear traveltime tomography*, Inverse Problems, 6, pp. 21-42.

[10] Berryman, J.G., 1989, *Weighted least-squares criteria for seismic traveltime tomography*, IEEE Trans. Geosci. Remote Sensing, 27(3), pp. 302-309.

[11] Berryman, J.G., 1989, *Fermat's principle and nonlinear traveltime tomography*, Phys. Rev. Let., 62(25), pp. 2953-2956.

[12] Berryman, J.G., 1991,*Convexity properties of inverse problems with variational constraints*, J. of Franklin Institute, vol. 328, no. 1, pp. 1-13.

[13] Borcea, L., Papanicolaou, G.C., 1996,*Network approximation for transport properties of high contrast materials*, submitted SIAM Applied Mathematics.

[14] Borcea, L., Papanicolaou, G.C., 1996,*A hybrid numerical method for high contrast conductivity problems*, submitted J. Computational and Applied Math..

[15] Borcea, L., Papanicolaou, G.C., Wehr, J., *Network approximation for high contrast random conductivities*, in preparation.

[16] Curtis, E.B., Morrow, J.A., 1990,*Determining the resistors in a network*, SIAM J. Appl. Math., Vol. 50, No. 3, June, pp. 931-941.

[17] Daily, W.D., A. Ramirez, D. LaBrecque and Nitao, J., 1992, *Electrical resistivity tomography of vadose water movement*, Water Resources Res. **28**, pp. 1429-1442.

[18] Dennis, J.E., Schnabel, R.B., 1996, *Numerical methods for unconstrained optimization and nonlinear equations*, SIAM.

[19] Dines, K.A., Lytle, R.J., 1981,*Analysis of electrical conductivity imaging*, Geophysics 46, pp. 1025-1036.

[20] Fletcher, R., 1987, *Practical methods of Optimization*, (New York: Wiley).

[21] Gill, P.E., Murray, W. and Wright, M.H., 1981,*Practical Optimization*, Academic Press, London.

[22] Habashy, T.M., Groom, R.W., Spies, B.R., 1993,*Beyond the Born and Rytov Approximations: A nonlinear approach to Electromagnetic Scattering*, J. Geophysical Research, Vol. 98, No. B2, pp. 1759-1755, February.

[23] Hestenes, M.R. and Stiefel, E., 1952, *Methods of conjugate gradients for solving linear systems*, J. Res. NBS **49**, pp. 409-436.

[24] Isakov, V., 1993,*Uniqueness and stability in multi-dimensional inverse problems*, Inverse Problems, 9, pp. 579-621.

[25] Ito, K. and Kunisch, K., 1990, *The augmented Lagrangian method for parameter estimation in elliptic systems*, SIAM J. Control **28**, 113–136.

[26] Jikov, V.V., Kozlov, S.M., Oleinik, O.A., 1994,*Homogenization of Differential Operators and Integral Functional*, Springer-Verlag, Berlin Heilderberg.

[27] Kaczmarz, S., 1937, Angenäherte Auflösung von Systemen linearer Gleichungen, *Bull. Acad. Polon. Sci. Lett.* **A**, pp. 355-357.

[28] Kitanidis, P.K., 1995,*Quasilinear Geostatistical Theory for Inversing*, Water Resources Res., 31, pp. 2411-2419.

[29] Kohn, R., Vogelius, M., 1985, *Determining conductivity by boundary measurements*, Comm. Pure App. Math., 38, pp. 643-667.

[30] Kozlov, S.M., 1989, *Geometric aspects of averaging*, Russian Math. Surveys 44:2, pp. 91-144.

[31] *LAPACK User's Guide,* 1992, SIAM.

[32] Levenberg, K., 1944, *A method for the solution of certain non-linear problems in least squares*, Quart. Appl. Math. **2**, pp. 164-168.

[33] Lu, Shin-yee and Berryman, J.G., 1990, *Inverse Scattering, Seismic Traveltime Tomography, and Neural Networks*, Int. J. of Imaging Systems and Techn., Vol. 2, pp. 112-118.

[34] Marquardt, D.W., 1963, *An algorithm for least-squares estimation of nonlinear parameters*, SIAM J. Appl. Math., **11**, pp. 431-441.

[35] Marquardt, D.W., 1970, *Generalized inverses, ridge regression, biased linear estimation, and nonlinear estimation*, Technometrics, **12**, pp. 591-612.

[36] Mallat, S. and Zhang, Z., 1993, *Matching pursuit in a time-frequency dictionary*, IEEE Trans. Signal Processing, **41**, pp. 3397-3415.

[37] McCormick, S.F. and Wade, J.G., 1993, *Multigrid solution of a linearized, regularized least-squares problem in electrical impedance tomography*, Inverse Problems, **9**, pp. 697-713.

[38] Mitchell, A.R., 1969, *Computational methods in partial differential equations*, J. Wiley, New York.

[39] Natterer, F., 1986, *The mathematics of computerized tomography*, John Wiley and Sons.

[40] Ramirez, A., Daily, D.W., LaBrecque, D., Owen, E. and Chesnut D., 1993, *Monitoring an underground steam injection process using electrical resistance tomography*, Water Resources Res., **29**, pp. 73-87.

[41] Rector, J.W., editor, 1995, *Geophysics*, Special Issue on Crosswell Methods, Vol. 60, No. 3.

[42] Santosa, F. and Vogelius., 1990, *A backprojection algorithm for electrical impedance imaging*, SIAM J. Appl. Math., **50**, pp. 216-243.

[43] Sylvester, J., Uhlmann, G., 1987, *A global uniqueness theorem for an inverse boundary value problem*, Ann. Math., 125, pp. 153-169.

[44] Sylvester, J., Uhlmann, G., 1990, *The Dirichlet to Neumann map and applications*, Inverse problems in partial differential equations, editors: Colton, D., Ewing, R., Rundell, W., SIAM, pp. 101-139.

[45] Tikhonov, A. and Arsénine, V., 1976, *Méthodes de Résolution de Problèmes Mal Posés*, Éditions Mir, Moscow.

[46] Yorkey, T.J., Webster, J.G. and Tompkins, W.J., 1987, *Comparing reconstruction algorithms for electrical impedance tomography*, IEEE Trans. Biomed. Engng., **34**, pp. 843-852.

[47] Zhou, Q., Becker, A., Morrison, H.F., 1993, *Audio-frequency electromagnetic tomography in 2-D*, Geophysics, pp. 482-495.